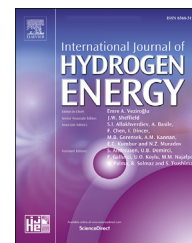


Available online at [www.sciencedirect.com](http://www.sciencedirect.com)

ScienceDirect

journal homepage: [www.elsevier.com/locate/he](http://www.elsevier.com/locate/he)

# Deep learning–assisted phase equilibrium analysis for producing natural hydrogen

Tao Zhang <sup>a,\*</sup>, Yanhui Zhang <sup>a</sup>, Klemens Katterbauer <sup>b</sup>,  
Abdallah Al Shehri <sup>b</sup>, Shuyu Sun <sup>a,\*\*</sup>, Ibrahim Hoteit <sup>a,\*\*\*</sup>

<sup>a</sup> King Abdullah University of Science and Technology, Saudi Arabia

<sup>b</sup> Saudi Aramco, Saudi Arabia

## ARTICLE INFO

### Article history:

Received 27 July 2023

Received in revised form

7 September 2023

Accepted 9 September 2023

Available online 26 September 2023

### Keywords:

White hydrogen

Phase equilibrium

Flash calculation

Thermodynamics-informed neural network

## ABSTRACT

The development of natural hydrogen is an emerging topic in the current energy transition trend. The production process involves compositional multiphase flow via subsurface porous media. This makes studying the compositional phase equilibrium behavior essential for reliable reservoir simulation and prediction. Herein, we develop an iterative flash calculation scheme and a deep learning algorithm using a thermodynamics-informed neural network (TINN) to perform accurate, robust, and fast phase equilibrium calculations for realistic fluid mixtures of natural hydrogen. The application of TINN architecture can accelerate the calculations for nearly 20 times. The effect of capillarity on phase equilibrium states is demonstrated. Based on simulation results, suggestions for the natural hydrogen industry chain are provided to control the possible phase transitions under certain environmental conditions that may be observed in the natural hydrogen reservoirs, storage and transportation facilities. The extremely low critical temperature of hydrogen challenges the robustness of flash calculations but facilitates the separation of impurities by liquefying certain undesired species. Moreover, phase transitions under control can be an effective approach for carbon dioxide capture and sequestration with optimized operating conditions over the phase equilibrium analysis.

© 2023 Hydrogen Energy Publications LLC. Published by Elsevier Ltd. All rights reserved.

## 1. Introduction

Developing clean and renewable energy and realizing energy transitions are important measures to reduce carbon dioxide emissions [1]. Today's world faces one major energy transition from carbon-containing to carbon-free energy (e.g., wind, solar, geothermal, and hydrogen) [2] to cope with climate change and reduce the impact on the environment via carbon

neutrality [3]. As a part of the global low-carbon technology portfolio, hydrogen profoundly influences the long-term reconstruction of the world's energy supply and application system. It facilitates the transition and generational evolution in transportation, power generation, chemicals, and construction [4]. Hydrogen has a minimal negative environmental impact as a desirable energy source because it only produces water during combustion. Hydrogen can be converted into electricity using fuel cells, reducing waste emissions [5]. It can

\* Corresponding author.

\*\* Corresponding author.

\*\*\* Corresponding author.

E-mail addresses: [tao.zhang.1@kaust.edu.sa](mailto:tao.zhang.1@kaust.edu.sa) (T. Zhang), [shuyu.sun@kaust.edu.sa](mailto:shuyu.sun@kaust.edu.sa) (S. Sun), [ibrahim.hoteit@kaust.edu.sa](mailto:ibrahim.hoteit@kaust.edu.sa) (I. Hoteit).  
<https://doi.org/10.1016/j.ijhydene.2023.09.097>

0360-3199/© 2023 Hydrogen Energy Publications LLC. Published by Elsevier Ltd. All rights reserved.

power heavy transportation with fewer emissions and high-temperature industrial operations that are difficult to electrify. Hydrogen's versatility makes it a pillar of energy transition policies.

Several color codes or nicknames have been coined within the energy industry to distinguish between different types of hydrogen based on how they are produced, including green, blue, gray, black, brown, yellow, turquoise, and pink hydrogen forms [6,7]. In the kaleidoscope of hydrogen colors, green hydrogen is produced with no harmful greenhouse gas emissions [8]. Green hydrogen is produced by electrolyzing water using clean electricity from surplus renewable energy sources, such as solar or wind power. Electrolyzers split water into its components of hydrogen and oxygen through an electrochemical reaction, emitting zero-carbon dioxide in the process [9]. Due to its high production cost, green hydrogen currently forms only a small percentage of the overall hydrogen production. However, with the decreased cost of wind energy [10], it is anticipated that the cost of green hydrogen will decrease as it becomes more widespread. Blue hydrogen is primarily produced from natural gas, using steam reforming, which combines natural gas and high-temperature steam [11]. Moreover, carbon capture and storage (CCS) [12] was implemented to mitigate carbon dioxide emissions. Therefore, blue hydrogen is sometimes described as low-carbon hydrogen. However, gray hydrogen remains the primary source of all produced hydrogen [13], which is produced from natural gas or other sources of methane, using steam reforming but without CCS. In the hydrogen spectrum, black and brown hydrogens are the opposite of green hydrogen and the most damaging to the environment. They allude to using black coal or lignite (brown coal) in hydrogen production [14]. Hydrogen obtained from fossil fuels through gasification is called black or brown hydrogen. Recently, Japan and Australia have announced a new brown coal-to-hydrogen project [15], which involves using brown coal in Australia to produce liquefied hydrogen, and then shipping the product to Japan for low-emission use. Pink hydrogen is generated using electrolysis powered by nuclear energy [16]. Nuclear-produced hydrogen can be called purple or red hydrogen [17]. Additionally, the very high temperatures produced by nuclear reactors could be applied to other hydrogen production to enable more efficient electrolysis or fossil gas-based steam methane reforming. Turquoise hydrogen is a new entry in the hydrogen color charts and production [18], generated using pyrolysis of methane with solid carbon as a by-product. Turquoise hydrogen may be potentially valued as low-emission hydrogen if the related thermal process is powered with renewable energy and the carbon can be permanently stored or utilized. Yellow hydrogen is a relatively new term for hydrogen made through electrolysis using solar power [19]. Note that there is no universal naming convention; these color definitions may change over time and even between countries.

White hydrogen, known as natural, geological, or native hydrogen, is reported in underground deposits [20]. It is a newly discovered sustainable geological source of energy. It is generated by a natural geochemical process deep inside the Earth's crust. Natural hydrogen is still a little-known energy source. Yet, certain projects are already established and

produce natural hydrogen in industrial quantities. In 2021, South Australia launched licenses for the specific prospection of white hydrogen. The South Australian Department of Energy and Mines (DEM) has deployed a project to identify natural hydrogen in South Australia and has issued hydrogen exploration permits. Golden Hydrogen, a company established in 2021, was granted a license by DEM to explore, evaluate, and develop natural hydrogen in the licensed area [21]. White hydrogen is believed to be an inexpensive solution to produce carbon-neutral hydrogen and competes economically with fossil fuels. Its industry chain is similar to natural gas production. It includes prospection, selection of sites, drilling, extraction, and separation of products. It is expected to be a more preferred hydrogen resource than the current, most inexpensive hydrogen produced by steam methane reforming (SMR) [22].

The hydrogen energy processes entail phase transitions. Therefore, phase equilibrium analysis is required for an accurate and reliable description of various engineering tasks in numerous scenarios involving temperature and pressure changes. White hydrogen development is no exception. Phase transition may occur during the white hydrogen's production, transportation, and storage, with a significant difference in the temperature, pressure, and container geometries. In particular, environmental conditions may fluctuate violently when the natural hydrogen flows from the subsurface porous reservoir to the production well. Moreover, liquefaction may occur when transported over a high-pressure long-distance pipeline, where the pressure can be larger than 10 MPa and certain components with a higher critical temperature than hydrogen may exist in the natural hydrogen production mixture. The extremely low temperature condition need also to be considered in certain scenarios in the natural hydrogen production chain, for example, storage in porous media, where the temperature can be less than 80 K. Thus, phase equilibrium analysis is essential to study white hydrogen. Furthermore, the influence of capillarity may drastically alter the phase properties while considering the white hydrogen depositing in and flowing through the subsurface porous reservoir, adding another barrier to the accurate description of the phase equilibrium states. The effect of capillarity on phase transitions of multi-component reservoir fluids flowing in porous media has been demonstrated in Ref. [23], but hydrogen has not been considered in the fluid mixtures. Thus, the effect of capillarity should be evaluated to guide the recovery of natural hydrogen.

Many studies have been reported in the past decades to study the phase equilibrium in the hydrogen energy industrial chain. These include modifying the phase equilibrium conditions for hydrogen sorption [24], controlling the hydrogen-metal systems for a better hydrogen storage capacity [25], studying the high-pressure gas cylinder to avoid the hydrogen effects under extreme conditions [26], economic and safety analysis for liquefied hydrogen storage and transportation in industrial scale [27], and many others [28,29]. The thermodynamically consistent phase equilibrium models developed based on the equation of states (EOS) have also been proposed to simulate the thermodynamic correlations among the environmental conditions and component properties during phase transitions that may happen in different application

scenarios, including hydrogen storage in NaCl brine [30] and alkane mixtures [31]. Besides the well-developed NPT (constant chemical composition (N), pressure (P), and temperature (T)) flash calculation method [32], the emerging NVT (constant chemical composition (N), volume (V), and temperature (T)) flash schemes [33,34] have been used to solve the thermodynamic models based on EOSs to obtain the phase equilibrium information [23]. The conventional iterative flash calculation schemes have been efficient in phase equilibrium studies in hydrogen energy; however, the computational cost is still a bottleneck if iterative methods are used [35]. In order to better study the thermodynamic mechanisms, a number of advanced methods have been proposed in recent years. Liu et al. used molecular descriptors (MD), molecular identifiers (MI), and combinations of MD and MI (MD\_MI) to represent the structure of ILs, combining pressure and temperature as the input of the model [36] to study environment-related gases [37]. Molecular structure encoding was applied in Ref. [38] to predict carbon dioxide solubility in ionic liquids. A method of separating azeotropes with organic-IL mixed extractant was proposed in Ref. [39] to discuss the structure-activity relationship between extractant and azeotrope. Qi et al. applied thermodynamic and techno-economic analyses on the hydrogen production processes from algae by plasma gasification [40]. First-principles [41] have also been incorporated in the microscopic description on complex molecular structures [42]. Structural and physical properties of hydrides have also been brought into researchers' attentions due to the high hydrogen storage capacities and low densities [43].

Recent advances in hardware equipment and computing power have enabled the hydrogen energy industry to pursue relatively higher precision and larger-scale standards for engineering computations. Ultra-large-scale engineering simulators designed to study the phase transitions in the hydrogen industry chain may benefit from accelerated computing of phase equilibrium states. Accordingly, emerging artificial intelligence technology and deep learning algorithms can accelerate physical and thermodynamic analysis [44]. Fan et al. studied a hybrid molecular descriptor combined with deep learning method to model and evaluate the rational application of ionic liquids (ILs) through deep convolutional neural networks (DCNN) [45]. Machine learning has also been effectively applied in the hydrogen production from steam methane reformer [46] and wastewater dark fermentation [47]. Recent studies suggested that the phase equilibrium prediction efficiency could be significantly enhanced while retaining the accuracy compared with the ground truth data, inspiring efforts to accelerate phase equilibrium calculations in the hydrogen industry [35]. As a relatively new resource in hydrogen energy, phase equilibrium studies in the natural hydrogen have not been extensively focused in previous publications. In particular, the effect of capillarity on the phase equilibrium status of white hydrogen, which is challenging to simulate in previous iterative flash calculation schemes, is expected to be represented efficiently in the deep learning model. Hydrogen storage is also a challenge due to the special physical properties of hydrogen [48,49], so that thermodynamic analysis on the phase and electrochemical properties of certain compounds [50], especially alloys [51], that can be used as batteries or storage containers have

emerged with the development of first-principle investigations in the past five years [52]. Deep learning techniques are also believed to be an effective approach to accelerate first-principle studies [53].

In this work, we propose to develop a thermodynamically consistent NVT flash scheme that can be applied in the phase equilibrium calculations in the white hydrogen development. Novelty of the proposed scheme is demonstrated on the thermodynamic consistency, as the whole algorithm is derived from the first and second law of thermodynamics. The effect of capillarity is incorporated into the model to characterize the phase properties effectively in the subsurface porous reservoir, as well as in the hydrogen storage scenario under extremely low-temperature conditions in porous media with nano-pores. A thermodynamics-informed neural network is established by training a deep learning model to accelerate phase equilibrium calculations. Based on the advanced network structure containing thermodynamic features, the basic thermodynamic rule has also been incorporated in formulating the loss function to make this algorithm more "thermodynamics-informed". The rest of this paper is organized as follows. The NVT flash scheme is introduced in Section 2, starting from the model construction and showing the practical application in the phase equilibrium calculations for two realistic white hydrogen fluids. The effect of capillary pressure is investigated in Section 3, describing the modifications to the numerical algorithm and changes in the phase equilibrium states. The deep learning algorithm is described in Section 4, demonstrating the performance of the trained model on both the phase stability test and phase-splitting calculation. Implications for the white hydrogen development are discussed in Section 5, together with the concluding remarks on future developments.

## 2. NVT flash calculation

### 2.1. NVT flash scheme

The first law of thermodynamics is used to model the energy conservation of the system, as demonstrated in the following Equation:

$$\frac{d(U + E)}{dt} = \frac{dW}{dt} + \frac{dQ}{dt} \quad (1)$$

where  $U$ ,  $E$ ,  $W$ , and  $Q$  represent the internal energy, kinetic energy, work done, and the heat transferred to the system, respectively. Considering the entropy definition, the change of the entropy of the surrounding environment,  $S_{\text{surr}}$ , can be calculated via:  $dS_{\text{surr}} = -\frac{dQ}{T}$ , and the entropy of the system,  $S_{\text{sys}}$ , can be determined by:  $S = S_{\text{sys}} + S_{\text{surr}}$ . Thus, the entropy changing with time can be formulated as follows:

$$\frac{dS}{dt} = \frac{dS_{\text{sys}}}{dt} + \frac{dS_{\text{surr}}}{dt} = \frac{dS_{\text{sys}}}{dt} - \frac{1}{T} \frac{dQ}{dt} = -\frac{1}{T} \frac{d(F + E)}{dt} + \frac{1}{T} \frac{dW}{dt} \quad (2)$$

where  $F$  is the Helmholtz free energy, which is minimized in the NVT type flash algorithm, instead of the Gibbs free energy, minimized in the NPT type flash algorithm.

For a gas-liquid two-phase system, the Helmholtz free energy can be calculated by:

$$F = f(n^G)V^G + f(n^L)V^L \quad (3)$$

where  $n$  denotes the molar density, and the superscripts  $G$  and  $L$  denote the gas and liquid phases, respectively. The Helmholtz free energy density, denoted by  $f$ , can be formulated as:

$$f(n) = f^{\text{ideal}}(n) + f^{\text{repulsion}}(n) + f^{\text{attraction}}(n) \quad (4)$$

where the three constituent energies are expressed as the following scheme based on Peng-Robinson equation of state:

$$\begin{aligned} f^{\text{ideal}}(n) &= RT \sum_{i=1}^M n_i (\ln n_i - 1) \\ f^{\text{repulsion}}(n) &= -nRT \ln(1 - bn) \\ f^{\text{attraction}}(n) &= \frac{a(T)n}{2\sqrt{2}b} \ln \left( \frac{1 + (1 - \sqrt{2})bn}{1 + (1 + \sqrt{2})bn} \right) \end{aligned} \quad (5)$$

for a fluid mixture with  $M$  components, where  $R$ ,  $a(T)$  and  $b$  denote the general gas constant, energy correction parameter and the volume correction parameter, respectively. Both  $a(T)$  and  $b$  are parameters from Peng-Robinson equation of state.  $a(T)$  denotes the attractive energy parameter changing with temperature, which is needed to describe the realistic thermodynamic rules as attractive van der Waals forces may be exhibited by real molecules if they are close to each other sufficiently.  $b$  denotes the volume parameter, which is needed as molecules may occupy a finite volume and thus reducing the physical volume that can be accessed by all molecules. The pressure can be a little higher compared with ideal “point molecules”.

For a multicomponent fluid mixture containing  $M$  components, the mixing rule of the two correction parameters can be given as follows:

$$\begin{aligned} a(T) &= \sum_{i=1}^M \sum_{j=1}^M y_i y_j (a_i a_j)^{1/2} (1 - k_{ij}) \\ b &= \sum_{i=1}^M y_i b_i \end{aligned} \quad (6)$$

where the binary interaction coefficients for the energy parameters  $a(T)$  are denoted by  $k_{ij}$  to model the interaction between the component  $i$  and component  $j$ . The compositional parameters for each component  $i$  can be calculated as described in Ref. [54].

Considering the conservation laws given by:

$$N^G + N^L = N^t, V^G + V^L = V^t \quad (7)$$

Thanks to the conservation law, at each time step  $t$ , the volume  $V^i$  and the molar composition  $N^i$  of each phase  $i$  can be arbitrarily chosen as the primary variable in a two-phase system, as the information of the other phase can be calculated using Equation (7). In this paper, we take the vapor phase as the primary phase, and the partial derivative of the free energy  $F(N^G, V^G)$  with respect to  $N_i^G$  and  $V^G$  can be expressed as below:

$$\begin{aligned} \frac{\partial F(N^G, V^G)}{\partial N_i^G} &= \mu_i(n^G) - \mu_i(n^L) = \mu_i^G - \mu_i^L \\ \frac{\partial F(N^G, V^G)}{\partial V^G} &= P(n^L) - P(n^G) = P^L - P^G \end{aligned} \quad (8)$$

where  $P$  denotes the pressure and  $\mu_i$  the chemical potential of component  $i$ . Thus, the time derivative of  $F(N^G, V^G)$  can be formulated using the chain rule as follows:

$$\begin{aligned} \frac{\partial F}{\partial t} &= \sum_{i=1}^M \frac{\partial F}{\partial N_i^G} \frac{\partial N_i^G}{\partial t} + \frac{\partial F}{\partial V^G} \frac{\partial V^G}{\partial t} = \sum_{i=1}^M (\mu_i^G - \mu_i^L) \frac{\partial N_i^G}{\partial t} \\ &\quad + (P^L - P^G) \frac{\partial V^G}{\partial t} \end{aligned} \quad (9)$$

where the time derivative of the mole  $\frac{\partial N_i^G}{\partial t}$  and that of volume  $\frac{\partial V^G}{\partial t}$  can be calculated using Onsager's reciprocal principle:

$$\begin{aligned} \frac{\partial N_i^G}{\partial t} &= \sum_{j=1}^M \psi_{ij} (\mu_j^G - \mu_j^L) + \psi_{i,M+1} (P^L - P^G) \\ \frac{\partial V^G}{\partial t} &= \sum_{j=1}^M \psi_{M+1,j} (\mu_j^G - \mu_j^L) + \psi_{M+1,M+1} (P^L - P^G) \end{aligned} \quad (10)$$

The Onsager coefficient matrix,  $\Psi = (\psi_{ij})_{i,j=1}^{M+1}$ , should be negatively definite to ensure the consistency with the second law of thermodynamics. Using the dynamic model formulated in Equation (10), the NVT flash calculation can be carried out from an initial state (non-equilibrium state) to an equilibrium state at the fixed moles, volume and temperature. At equilibrium,  $P^L - P^G$  is expected to be 0.

## 2.2. Application in white hydrogen development

As early as 1888, a study analyzed the gas composition of natural hydrogen samples leaked from coal seams in the coal mines near Makiivka, Ukraine [55], believed to be the first official discovery of white hydrogen. Recently, 331 onshore hydrogen analysis data were reviewed by Zgonnik [56], confirming that natural hydrogen is widely distributed in the world, including America, Europe, Asia, Africa, Oceania, and other regions, but its content varies from 1% to 100% in different regions and geological settings. This paper used two natural hydrogen fluids as the sample gas to study the phase equilibrium characteristics, namely the Robe1 gas and the Ramasay1 gas.

The Robe1 gas was sampled from the Robe1 well (drilled in 1915 in the Otway Basin), and analyzed by the Department of Chemistry in Australia, recording anomalous hydrogen content [57]. As outlined in Table 1, five major components are observed in the gas mixture: hydrogen, oxygen, carbon dioxide, methane, and nitrogen. Methane, nitrogen, and hydrogen make the majority content, larger than 90%, estimated by the summation of mole fraction ( $z_i$ ), whereas carbon dioxide and oxygen comprise only 4.3% of the total compositions. The critical temperature  $T_{c,i}$ , critical pressure  $P_{c,i}$  and acentric

**Table 1 – Mole fractions and compositional parameters for the Robe1 gas.**

Component	$z_i$	$T_{c,i}$ (K)	$P_{c,i}$ (MPa)	$\omega_i$
H <sub>2</sub>	0.254	33.14	1.2960	−0.2190
O <sub>2</sub>	0.03	154.2	5.0800	0.0222
CO <sub>2</sub>	0.013	304.11	7.3739	0.2250
CH <sub>4</sub>	0.396	190.56	4.5988	0.0110
N <sub>2</sub>	0.307	126.22	3.3943	0.0400



factor  $\omega_i$  of each component are also provided to proceed with the flash calculation. As the mole fraction of oxygen and carbon dioxide is relatively small, the two species are combined as one component, marked as carbon dioxide, in this study to simplify the computations and illustrations. The binary interaction parameters among the species can be found in Ref. [58]. NVT flash involving capillarity is believed to improve the flow and transport simulation accuracy of the multicomponent and multiphase fluid in porous media.

The tangent plane distance function (TPD) is one popular index indicating the phase stability of the system at certain environmental conditions, thereby informing the number of phases at equilibrium. Several reformulations have been proposed to calculate the TPD function to fit various application scenarios [59,60]. In this work, the following equation is used to calculate the TPD value for the Helmholtz free energy surface to keep consistent with the NVT flash condition [43]:

$$D_E(d) = \sum_{i=1}^{nc} d_i [\mu_i(d) - \mu_i(d_0)] - (p(d) - p(d_0)) \quad (11)$$

where  $D_E(d)$  denotes the TPD corresponding to the Helmholtz free energy density  $E$ , and  $d$  represent the vector of component molar densities.

The phase stability test of the Robe1 gas within the temperature range of [100 K, 300 K] and the total molar density range [0, 480 mol/m<sup>3</sup>] is presented in Fig. 1, with the corresponding TPD function plotted as the reference. A two-phase region can be detected in the low-temperature area, where TPD is negative, indicating unstable phase conditions. As the temperature increases, the TPD function rises to 0, and the phase conditions are stable so that phase transition is not expected to occur. Thus, only one single phase remains under certain conditions at equilibrium. Moreover, reducing the total molar density at the same temperature can also make the system stable in the single-phase region at equilibrium. In general, a smaller total molar density and a higher temperature can drive the fluid mixture to change from liquid to vapor phase with a specific container volume, helping the system move from the vapor-liquid two-phase region to the single-vapor-phase region [61,62]. Thus, the phase stability test result meets well with the theoretical inference, validating the physical plausibility of the flash scheme developed in this paper.

Based on the phase stability test, phase splitting calculations can provide information on the mole fractions of each component in each phase. The gasified mole fraction of each component in the mixture at constant  $C = 96$  mol/m<sup>3</sup> in the Robe1 gas mixture is plotted in Fig. 2. As shown in the curves, the gasified mole fraction of methane first increases swiftly from 0.85 to 0.99 with the temperature increasing from 100 K to 113.8 K, then slowly approaching 1 until 169 K. Meanwhile, increasing the temperature from 100 K to 169 K increases the mole fraction of carbon gradually from 0 to 1. However, the mole fraction of hydrogen and nitrogen almost maintained as 1 within the same temperature range, indicating that the two components remain in the single-vapor-phase region for temperatures higher than 100 K, and the total molar density is constant at 96 mol/m<sup>3</sup>. Such a finding can be explained by the different critical temperatures of each component. Among these, the critical temperature of hydrogen is the lowest, and that of carbon dioxide is the highest. Thus, the natural hydrogen production of the Robe1 well can be purified to remove all the carbon dioxide (and oxygen) and some of the methane impurities in the liquid phase if the temperature is maintained at 100 K under such a total molar density. It is reasonable to anticipate that more methane and nitrogen can be removed if we reduce the temperature. Hydrogen has the smallest critical temperature in the four components and, thus, is the most difficult to be liquidized.

The compositional mole fraction in the vapor phase at the constant total molar density of 96 mol/m<sup>3</sup> can be computed, as shown in Fig. 3. With increasing temperature, methane will be gasified first and then carbon dioxide, which results in the increasing mole fraction of methane and carbon dioxide in the vapor phase. When the total mixture enters the single-vapor-phase region, the compositional mole fraction in the vapor phase of all the components will be the same as the feed compositions due to mass conservation.

At a larger total molar density, the phase behaviors should differ as environmental conditions change. Fig. 4 suggests that at constant  $C = 192$  mol/m<sup>3</sup>, the gasification of methane and carbon dioxide slows down compared with the curve in Fig. 2. This result is attributed to a larger pressure in the domain at the same temperature. Moreover, the phase transition from liquid to vapor phase can also be observed for the nitrogen component, shown by the ascent in the green curve, and

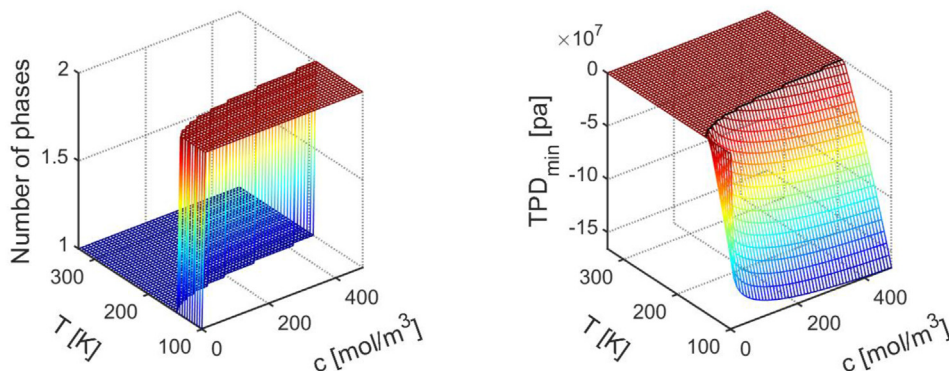
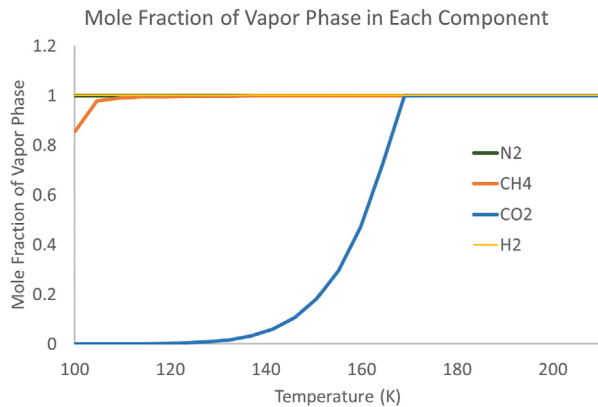


Fig. 1 – Number of phases at equilibrium (left) and the TPD function (right) of the Robe1 gas.



**Fig. 2 – Gasified mole fraction of each component at constant  $C = 96 \text{ mol/m}^3$  in the Robe1 gas.**

differs significantly from the flat green curve in Fig. 2. A higher temperature is required for the mixture to enter the single-phase region, 178.2 K, compared with 169 K in Fig. 2. Thus, more methane and nitrogen impurities can be removed from the white hydrogen production fluid by removing the liquid phase at a larger total molar density, which can be achieved by controlling the flux through and the container volume of the separator. Meanwhile, under a constant environment volume, a larger total molar density may result in a larger pressure, which indicates that more methane and nitrogen impurities can be removed by the controlled liquefaction using pressure increasing techniques. Similarly, for a production fluid with a constant flux, reduction in the container volume may result in a larger total molar density, which may also help to remove the impurities of the production.

Another white hydrogen mixture is used as the sample gas, Ramsay1, to validate the general applicability of the studied flash scheme. Hydrogen has also been detected in the wells in Minlaton Oil Syndicate Bore1 (Ramsay Oil Bore1, also referred to as Minlaton Oil Bore [63]) drilled on the central Yorke Peninsula, which recorded high percentages of hydrogen. Table 2 shows that the mole fraction of hydrogen is higher than 60%, while nitrogen takes almost a quarter of the total composition. The methane content is much smaller than that in Robe1 gas, and carbon dioxide and oxygen still make the

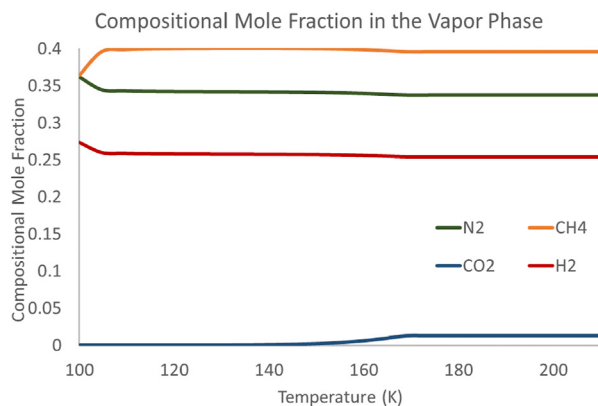


**Fig. 3 – Compositional mole fraction in the vapor phase at constant  $C = 96 \text{ mol/m}^3$  in the Robe1 gas.**

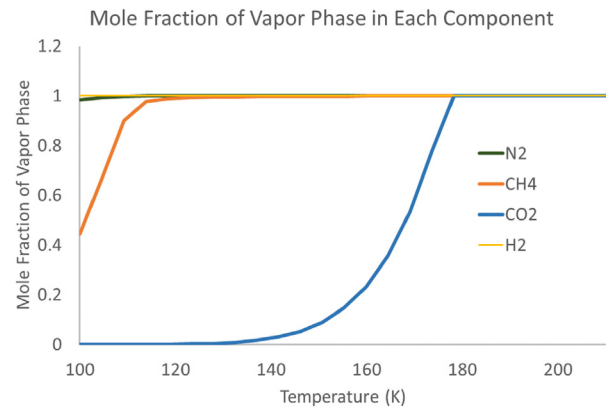


**Fig. 4 – Gasified mole fraction of each component at constant  $C = 192 \text{ mol/m}^3$  in the Robe1 gas.**

smallest part. Thus, in this study, methane, carbon dioxide, and oxygen are combined into one component for investigating Ramsay1 gas and marked as methane in the following context to facilitate computations and illustrations.

The phase stability test of the Ramsay1 gas within the temperature range of [50 K, 330 K] and the molar density range [0, 4800 mol/m<sup>3</sup>] is presented in Fig. 5, with the corresponding TPD function plotted as the reference. A larger range of temperature and pressure conditions can be included in this scenario, in order to test the robustness of the proposed method. The large range of temperature and pressure conditions can also meet the requirements of extreme conditions that may be needed in the natural hydrogen industry chain. For example, the temperature can be less than 100 K in the hydrogen storage in the porous media. The pressure corresponding to certain molar density range can also exceed 100 MPa, to meet the environment conditions of pipeline transportation under high pressures. As hydrogen becomes the dominant component and its critical temperature is very low, a smaller two-phase region is observed compared with Fig. 1. This indicates that it is easier for the production mixture of Ramsay1 gas to be stable in the single-vapor-phase region and avoid phase transition, which may facilitate production and transportation.

Further, the gasified mole fraction of each component at constant  $C = 960 \text{ mol/m}^3$  in the Ramsay1 gas is calculated and the results are shown in Fig. 6. The corresponding compositional mole fraction in the vapor phase is shown in Fig. 7. Comparatively, a much lower temperature is required for the Ramsay1 gas mixture to enter the single-vapor-phase region, 111.6 K, even at a much larger total molar density compared with the Robe1 gas. The increase in temperature from 50 K to

**Table 2 – Mole fractions and compositional parameters for the Ramsay Oil Bore1 production.**

Component	$z_i$	$T_{c,i}(\text{K})$	$P_{c,i}(\text{MPa})$	$\omega_i$
H <sub>2</sub>	0.644	33.14	1.2960	−0.2190
O <sub>2</sub>	0.024	154.2	5.0800	0.0222
CO <sub>2</sub>	0.008	304.11	7.3739	0.2250
CH <sub>4</sub>	0.07	190.56	4.5988	0.0110
N <sub>2</sub>	0.254	126.22	3.3943	0.0400

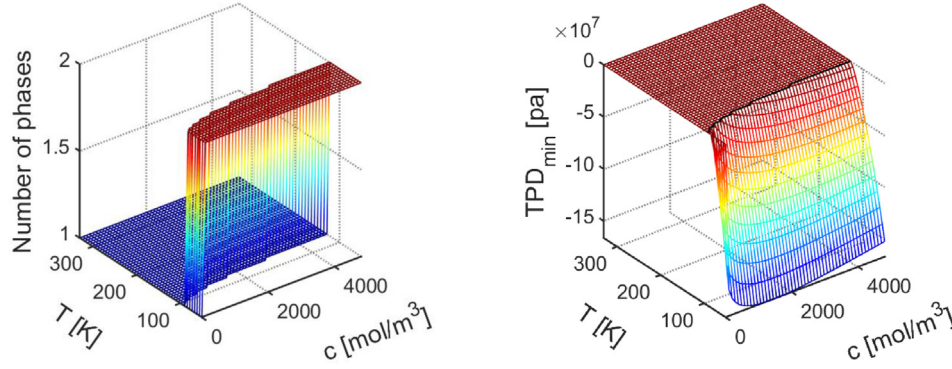


Fig. 5 – Number of phases at equilibrium (left) and the TPD function (right) for the Ramsay1 gas.

111.6 K causes a significant increase in the gasified mole fraction of methane and nitrogen, whereas the opposite behavior is observed for the hydrogen. Thus, reducing the system temperature from 111.6 K to 50 K can help remove the liquefied methane first, followed by the liquefied nitrogen, to purify the hydrogen production. Moreover, suppose we want to ensure the safe transportation of the produced gas mixture in the vapor phase to avoid unexpected liquefaction. In that case, the temperature should be kept higher than 111.6 K and the total molar density constant at 960 mol/m<sup>3</sup>.

As analyzed for the Robe1 gas, if the total molar density of the system is increased, a higher temperature is required for the gas mixture to keep stable in the single-vapor-phase region. As shown in Fig. 8, similar to the Ramsay1 gas, if one increases  $C$  from 960 mol/m<sup>3</sup> to 1920 mol/m<sup>3</sup>, a larger two-phase region can be observed with a higher temperature compared with Robe1 gas, 122.8 K, to enter the single-vapor-phase region. The increase in the gasified mole fraction of methane and nitrogen slows down as a larger pressure is effective in the system in this case.

### 3. Effect of capillary pressure

Capillary phenomena are crucial in multiphase systems involved in many reservoir and chemical engineering

problems. Capillary pressure is one of the most important driving forces for multiphase flow in porous media, especially in fractured media. Capillary action is often considered the dominant mechanism for oil and gas production in fractured reservoirs [63]. Thus, capillary pressure is significant for white hydrogen production. As capillarity can substantially change the phase characteristics, capillary pressure has gradually been applied to the phase equilibrium calculation models under NPT conditions [64] and thus should also be considered under NVT conditions. Furthermore, NVT flash involving capillarity is believed to improve the thermodynamic consistency of the flow and transport simulation of the multicomponent and multiphase fluid in porous media. Considering the presence of capillarity pressure, NVT conditions can be generated more directly as the pressure is not a constant in the system. This is because the capillary effect is generally regarded as one of the most important Darcy-scale phenomena produced by the liquid-gas interface at the pore scale. Consequently, a study on the effect of capillary pressure is essential for the multi-scale modeling and simulation of white hydrogen flow and transport through the subsurface porous media.

Because of the capillarity effect, a pressure difference exists at the contact between the gas and the liquid phases, which is known as capillary pressure, denoted by  $p_c$ . It is defined as the difference between the gas phase pressure,  $p_g$ , and the liquid phase pressure,  $p_l$ , i.e.,

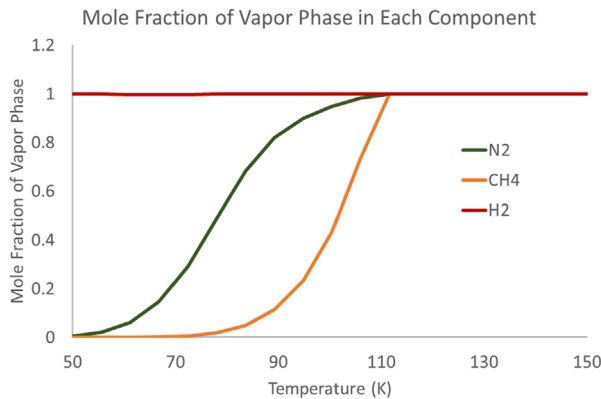


Fig. 6 – Gasified mole fraction of each component at constant  $C = 960$  mol/m<sup>3</sup> in the Ramsay1 gas.

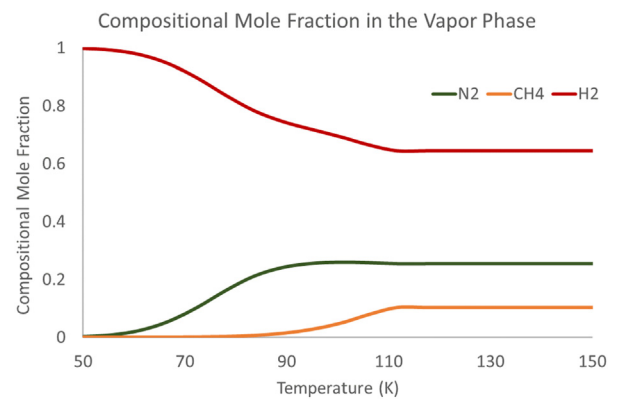
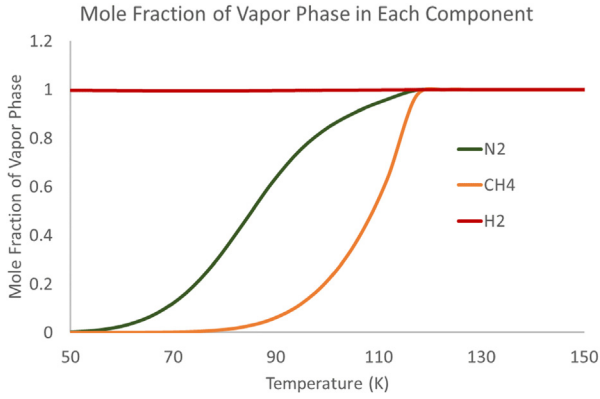


Fig. 7 – Compositional mole fraction in the vapor phase at constant  $C = 960$  mol/m<sup>3</sup> in the Ramsay1 gas.



**Fig. 8 – Gasified mole fraction of each component at constant  $C = 1920 \text{ mol/m}^3$  in the Ramsay 1 gas.**

$$P_c = P_G - P_L \quad (11a)$$

For two-phase fluid flow in porous media, the capillary pressure is usually determined by a semi-empirical formula related to the specified phase saturation [65]. Capillary pressure usually depends on various thermodynamic variables and physical properties, such as temperature, molar density, pore size, and contact angle. Here, one uses the Young–Laplace equation [66] and the Weinaug–Katz correlation [67] to model the capillary pressure at the pore scale to account for the general capillary effect that can reflect geological and environmental conditions. The Young–Laplace equation can be written as follows:

$$P_c = \frac{2\sigma \cos\theta}{r} \quad (12)$$

where  $\sigma$  is the interfacial tension, which can be calculated using the Weinaug–Katz correlation [68] as:

$$\sigma^{1/4} = \sum_{i=1}^M [P]_i (n_i^L - n_i^G) \quad (13)$$

In the above scheme,  $\theta$  is the contact angle,  $r$  is the pore size, and  $[P]$  is the parachor [50]. Further, the work done by the capillary pressure should be considered in the energy conservation law to keep consistent with the laws of thermodynamics and can be modeled as:

$$\frac{dW_c}{dt} = - \int_I p_c \mathbf{u} \cdot \mathbf{v} dI \quad (14)$$

where  $t$  is the time,  $\mathbf{u}$  is the velocity on the contact surface,  $\mathbf{v}$  is the normal unit outward vector to  $I$ , and  $I$  is the contact region between the vapor and liquid two phases. Based on the assumption that  $p_c$  remain constant on the interface and  $\mathbf{u}$  is a constant vector parallel along the container towards from liquid to gas, using the divergence theorem

$$\int_I \mathbf{u} \cdot \mathbf{v} dI - \int_A \mathbf{u} \cdot \mathbf{v} dA = 0 \quad (15)$$

where  $A$  is the cross-sectional area of the container of the system, Equation (14) can be further simplified for a flat surface as below:

$$\frac{dW_c}{dt} = - p_c \mathbf{A} \cdot \mathbf{v} = - p_c \frac{dV^G}{dt} \quad (16)$$

Thus, the time derivatives modeled in Equation (10) can be updated as the following scheme to include the effect of capillary pressure

$$\frac{\partial N_i^G}{\partial t} = \sum_{i=1}^M \psi_{ij} (\mu_j^G - \mu_j^L) + \psi_{i,M+1} (P^L - P^G + p_c) \quad (17)$$

$$\frac{\partial V^G}{\partial t} = \sum_{i=1}^M \psi_{M+1,j} (\mu_j^G - \mu_j^L) + \psi_{M+1,M+1} (P^L - P^G + p_c)$$

Using the dynamic model formulated in Equation (17), the dynamic process from an initial non-equilibrium state to the equilibrium state in the presence of capillary effect can be carried out in the NVT flash scheme.

The phase equilibrium states of the Ramsay1 gas can be studied using the updated scheme considering the effect of capillary pressure for a more accurate simulation at a specific mole number, volume, and temperature, e.g., NVT conditions. In fact, as nano-pores have been observed in the hydrogen storage materials, the effect of capillary pressure is important in the natural hydrogen industry chain. Fig. 9 depicts that the phase stability of the gas mixture changes significantly when the capillary pressure is included. Generally, the transition from the vapor-liquid two-phase region to the single-vapor-phase region is postponed when a higher temperature is required. This observation is consistent with the conclusion in Ref. [69] that the dew point curve should expand with the capillary pressure. At the constant  $C = 1920 \text{ mol/m}^3$ , 117.2 K is needed for the Ramsay1 gas mixture to enter the single-phase region if no capillary pressure is considered. However, 122.8 K is needed if the capillary pressure is considered with the pore radius ( $r$ ) of 10 nm or 5 nm. Moreover, the various capillary effects with different pore radii can be detected from the phase stability test results. For a large pore radius ( $=100 \text{ nm}$ ), the number of phases remains the same as the no capillarity conditions (as shown in the red diamonds and orange curve), which indicates that the capillary effect can be ignored for large pore sizes. This finding meets well with the classical oil and gas reservoir simulation theories, in which the capillary effect is usually demonstrated in shale or tight reservoirs with small pore sizes [23]. Similarly, for the white hydrogen fluid

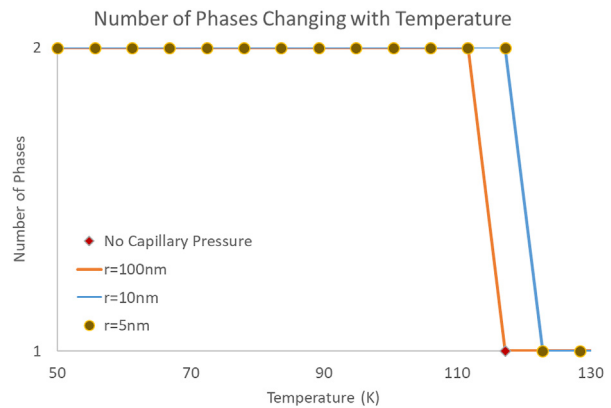


**Fig. 9 – Effect of capillary pressure on the number of phases at equilibrium at constant  $C = 1920 \text{ mol/m}^3$  in the Ramsay1 gas.**



flow in the subsurface porous media, the capillary effect is more crucial if the reservoir is tight, for example, shale-type reservoirs [70].

In addition to the phase stability test, the effect of capillary pressure on the phase splitting states can be captured from the mole fraction of the vapor phase in each component. As shown in Fig. 10, the mole fraction of the vapor phase in the N<sub>2</sub> component is predicted under different geological conditions at constant  $C = 1920 \text{ mol/m}^3$ . With increasing the temperature, more N<sub>2</sub> will be gasified, and the mole fraction of the vapor phase will increase. As observed from the smaller single-vapor-phase region, the vapor phase mole fraction increase will be slowed if the capillary pressure is considered. Furthermore, compared with a larger vapor phase mole fraction at  $r = 10 \text{ nm}$ , the effect of pore radius on the capillarity is more significant with a smaller vapor phase mole fraction at  $r = 5 \text{ nm}$  under the same temperature. The capillary effect at  $r = 100 \text{ nm}$  is negligible, which makes no difference from that under no-capillarity conditions, as shown by the red diamonds and orange curves. Such a rule can be inferred from Equation (12), which validates the reliability of the numerical scheme. The role of capillary pressure in phase equilibrium is always believed to be the suppression of bubble point curve and expansion of the dew point curve [36], which can also be referred from Fig. 10.

#### 4. Deep learning algorithm

Artificial neural networks (ANN) have been used effectively in the phase equilibrium studies of hydrocarbon mixtures to act as a computational model that can unearth the underlying thermodynamic rules [35]. In this work, we have established a thermodynamics-informed neural network (TINN) [69] to improve the representational ability of the neural network to better recover the thermodynamic rules underneath the phase equilibrium processes in the white hydrogen industry chain.

As shown in Fig. 11, the thermodynamic features of each component, including the critical temperature and pressure, acentric parameter, and feed composition, are selected as the indices to label each component. Further, the environmental conditions, such as the temperature, total molar density, and

the pore size determining the capillary effect, are used as the input features. Both phase stability test and phase splitting calculations are incorporated into this network by outputting the number of phases at equilibrium and the compositional mole fractions in each phase simultaneously. In conventional iterative flash calculation algorithms, both the phase stability and phase splitting results are calculated by a numerical scheme, in which the thermodynamic features are used as known parameters. The thermodynamic rules controlling the phase transition are described by the thermodynamic models, usually formulated based on the equation of states [71]. In the proposed deep learning algorithm using the TINN architecture, certain rules are represented by the combination of the many nodes and connections in the neural network. The non-linear flash model has been replaced by a linear model consisting of the trained weight parameters in the network, which makes the phase equilibrium calculation more direct and robust. In addition to the advanced network architecture containing thermodynamic information, the algorithm is further “thermodynamics-informed” by modifying the loss function with basic thermodynamic rules. In details, the loss function generated in Ref. [35].

$$L = \frac{1}{N} \sum_{n=1}^N \|\mathbf{o} - \hat{\mathbf{o}}\|^2 + \lambda \|\mathbf{W}\|_2^2 \quad (18)$$

is optimized as

$$L = \frac{1}{N} \sum_{n=1}^N \|\mathbf{o} - \hat{\mathbf{o}}\|^2 + \lambda \|\mathbf{W}\|_2^2 + \sum_{i=1}^M X_i + \sum_{i=1}^M Y_i - 2 \quad (19)$$

where  $L$  denotes the loss function,  $N$  the number of training data,  $\mathbf{o}$  the ground truth data,  $\hat{\mathbf{o}}$  the model prediction,  $\lambda$  the regularization coefficient of the L2 weight decay term,  $\mathbf{W}$  the weight parameters and  $M$  the number of components.  $X_i$  and  $Y_i$  denote the mole concentration of each component  $i$  in the liquid and gas phase, respectively. Obviously, the conservation rules  $\sum_{i=1}^M X_i = 1$  and  $\sum_{i=1}^M Y_i = 1$  have been incorporated to improve the thermodynamic consistency during the loss function decay process in the training of the deep learning model.

Considering the complexity of the phase equilibrium problems and the resultant large number of nodes needed for an accurate deep learning model, the dropout technique [72] is adapted. This technique reduces the degree of freedom of the model in training by discarding some nodes in the network to eliminate the corresponding connection relationship, as shown by the dotted nodes in Fig. 11. In addition to adding the code of selecting and discarding certain nodes in each batch in the training program, the dropped nodes will be put back to the network architecture after each batch to improve the robustness and consistency. Besides, batch normalization [73] and Xavier initialization [74] are applied to improve the training efficiency for such a complex problem of high-dimensional nonlinear relations. As it is expensive to obtain enough experimental data for training and validation in the deep learning algorithm, the ground truth data is prepared using the iterative flash calculation scheme as proposed above. In order to provide a data set carrying enough information for a better training and validation, totally 5041 data points are prepared within the temperature range of [50 K, 330 K] and the

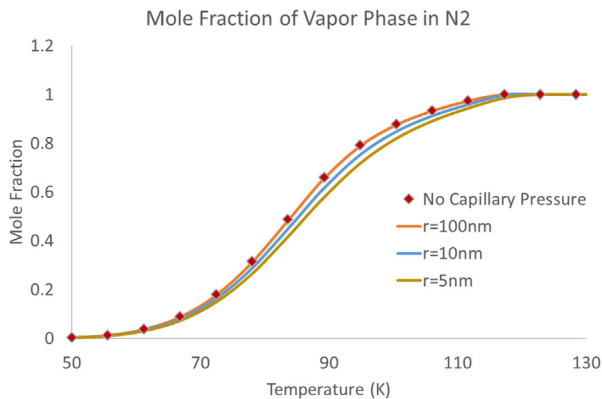


**Fig. 10 – Effect of capillary pressure on the mole fraction of the vapor phase in the N<sub>2</sub> component at constant  $C = 1920 \text{ mol/m}^3$  in the Ramsay1 gas.**

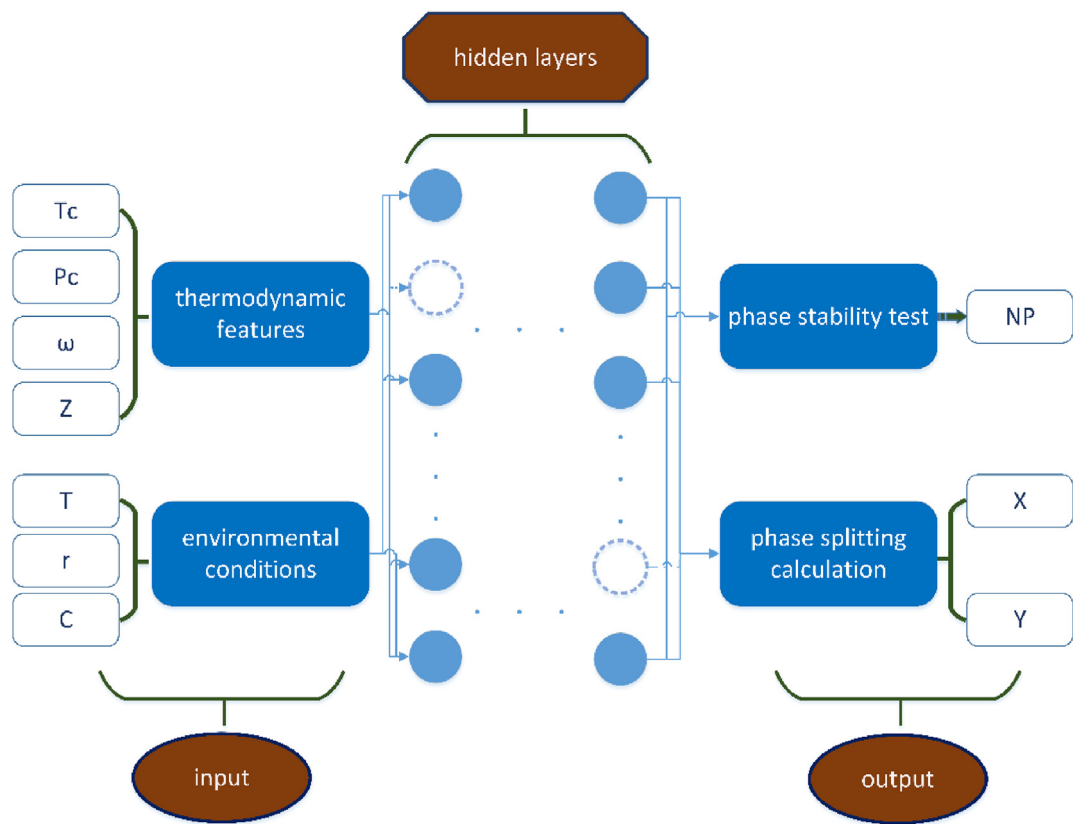


Fig. 11 – Schematic of the thermodynamics-informed neural network (TINN) architecture.

molar density range [0, 4800 mol/m<sup>3</sup>]. After obtaining the ground truth data, 80% of the data is used for training the model, while other 20% is used for validation and testing. In that way, the data for validating the model is “new” to the trained model, which makes the validation meaningful to prove the accuracy of the model.

The main purpose of applying deep learning techniques here is to accelerate the computation and save CPU time. As shown in Fig. 12, the CPU time needed for phase equilibrium calculation is compared between the iterative flash method and the deep learning model. The results indicate that the model trained by deep learning can considerably improve the

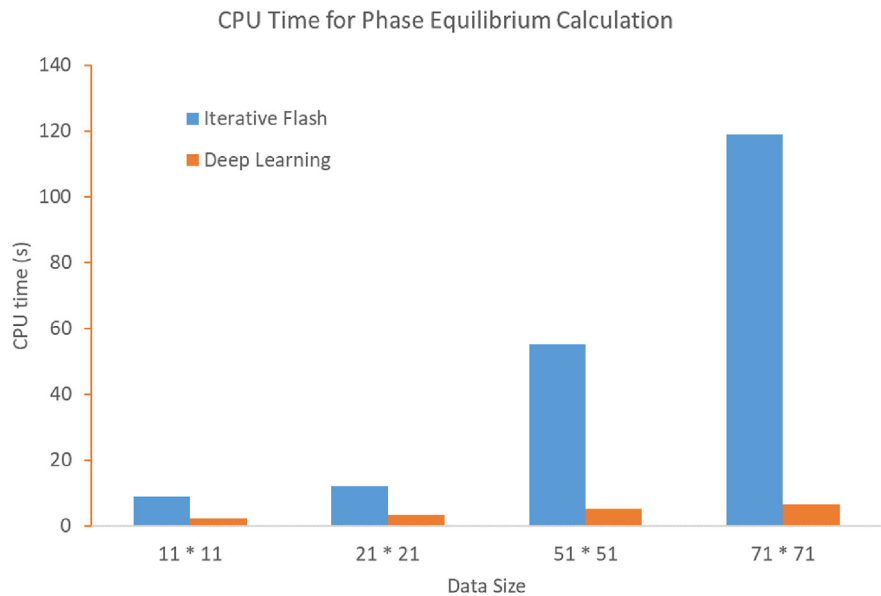
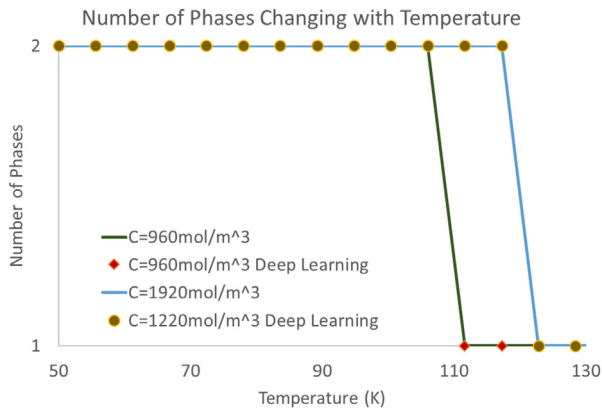


Fig. 12 – Comparison of the computational time used for phase equilibrium calculation using an iterative flash algorithm and deep learning algorithm.



**Fig. 13** – Deep Learning prediction on the phase stability test in the Ramsay1 gas at constant  $C = 960 \text{ mol/m}^3$  and  $C = 1920 \text{ mol/m}^3$ .

phase equilibrium calculation efficiency, especially for a large data set, as listed on the x-axis. For the  $71 \times 71$  data size, namely, 5041 phase equilibrium data points at 71 temperatures with 71 total molar densities, only 6.5 s is required to obtain the phase equilibrium data using the trained deep learning model, whereas 118.9 s is needed if the iterative scheme is applied.

Besides improving the computational efficiency, the prediction accuracy of the deep learning model should be preserved to be applied in the white hydrogen processes. The phase stability is first tested using the trained model, and the results are compared with the iterative flash data. As shown in Fig. 13, with increasing temperature, the Ramsay1 gas mixture changes from the two-phase region to the single-vapor-phase region, with the number of phases changing from 2 to 1. Moreover, a larger overall mole density will cause a higher temperature entering the single-vapor-phase regions, as a corresponding larger pressure may easily cause liquefaction. The reliability of the deep learning algorithm is validated because its prediction matches the ground-truth data, i.e., the iterative flash calculation. The trained deep learning model can accurately capture the phase transition temperature in both cases under different environmental conditions. Moreover, the deep learning model can also output the phase-splitting calculation, which is evaluated by comparing it with the ground-truth data. As shown in Fig. 14, the trained model can well predict the compositional mole fraction of all the components in the vapor phase of Robe1 gas under a constant total molar density of  $192 \text{ mol/m}^3$  and well capture the phase transition. For example, the mole fraction of carbon dioxide will increase first and becomes flat after entering the single-vapor-phase region. The unchanged compositional fraction in the vapor phase remains the same as the feed composition for the gas mixture, which is reasonable as only a single phase exists in the mixture under certain conditions.

Based on the deep learning predictions, the natural hydrogen industry can quickly obtain a basic knowledge of the thermodynamic conditions of the natural hydrogen mixture, which may help them facilitate the decision-making process in the reservoir monitoring, purification, storage and transportation. For example, if unwanted

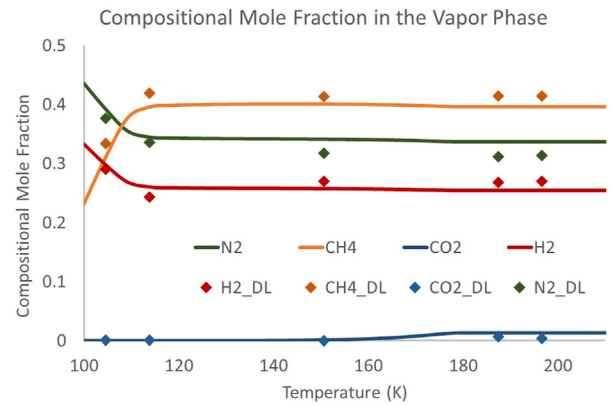


**Fig. 14** – Deep Learning prediction on the compositional mole fraction in the vapor phase at constant  $C = 192 \text{ mol/m}^3$  in the Robe1 gas.

liquefaction may occur under certain conditions as predicted by the deep learning model, the engineer may reduce the pressure or improve the temperature condition to keep the natural hydrogen production mixture in the single-vapor-phase region. The validity of the proposed deep learning algorithm is proved to be reliable in extreme conditions, including a very low temperature as 50 K, which can meet the requirements of low-temperature hydrogen storage in porous media and other engineering scenarios. Furthermore, as the thermodynamic properties have been involved in the network architecture, the components in the mixture can vary with different scenarios and be represented well using the thermodynamic features, which reduces the cost of repeated re-training.

## 5. Conclusion

Phase equilibrium analysis is essential for accurately and reliably describing various engineering tasks during the production of white or natural hydrogen. The phase equilibrium states of the white hydrogen fluid mixture were studied herein, first using an iterative NVT flash calculation scheme and then accelerated using a deep learning algorithm. In particular, the effect of capillarity on phase equilibrium states is investigated to guide the production of white hydrogen flowing through subsurface porous media, as white hydrogen may exist in shale reservoirs. Two realistic white hydrogen samples were studied to determine the potential applications of controlling the phase transition while purifying hydrogen production. Both the phase stability test and phase splitting calculations are performed. The robustness of both methods is validated by accurately predicting the phase equilibrium conditions within a wide temperature range with temperatures as low as 50 K and as high as 330 K to fit the extremely low critical temperature of hydrogen and the requirements of practical engineering processes in hydrogen production, purification, storage and transportation. The 20-times fast phase equilibrium calculation achieved using the TINN network architecture and the associated deep learning techniques has been demonstrated for large datasets, suggesting the potential

to be applied in large-scale compositional fluid simulators for white hydrogen development. The developed accurate, robust and fast phase equilibrium calculation scheme aided by deep learning techniques can be directly used in hydrogen industry for a better production, purification and transportation, as well as to be used as a thermodynamically-consistent initial phase distribution of multi-phase flow simulations in the whole natural hydrogen industry chain.

Based on the presented results, the following remarks can be made for better production economics and safety while developing white hydrogen.

1. The effect of pore sizes on capillarity can direct the natural hydrogen production by adjusting the working conditions according to the phase equilibrium calculation under different geological formations, e.g., to ensure a single-phase flow in the subsurface porous media, or to separate the liquefied carbon dioxide for further carbon capture and sequestration purposes.
2. The phase equilibrium calculations can be applied in the purification of white hydrogen production by removing the impurities, including methane, nitrogen, and carbon dioxide, using phase transitions under control. Hydrogen's extremely low critical temperature facilitates the purification because there remains a large temperature region within which only hydrogen cannot be liquefied. Suppose one wants to keep certain impurities in the gas production for easier transportation or safer storage. In that case, the mixture should be kept stable under specific environmental conditions to avoid the undesired liquefaction of nitrogen or methane.
3. The TINN scheme developed for phase equilibrium simulations could be combined with other deep learning algorithms designed for fluid flow simulation. For example, a physics-informed neural network (PINN) [75] establishes a complete simulator that can simulate the multicomponent and multiphase flow in the development of white hydrogen.
4. The effect of dynamic sorption on phase equilibrium states can also be incorporated in future studies, for a more accurate description of the phase behaviors in shale-type natural hydrogen reservoirs.
5. Hydrides are playing an increasingly important role in the storage and transportation of hydrogen [41]. Considering the complex physical and chemical processes that may be involved in the formation and workflow of hydrides, molecular dynamics simulation algorithms may be needed in future studies to investigate the phase transitions of hydrides.
6. Irreversible entropy production may also be taken into account in the following work to further improve the description of the realistic thermodynamic processes in practical natural hydrogen industry chain.

### Declaration of competing interest

The authors declare that they have no known competing financial interests or personal relationships that could have appeared to influence the work reported in this paper.

### Acknowledgment

This work was supported by the Office of Sponsored Research (OSR) at King Abdullah University of Science and Technology (KAUST) and by the Saudi Aramco-funded project "AI-aided Probabilistic Reservoir Characterization Using Ensemble History Matching and Big Data" (Grant No. RGC/3/4290-01-01).

### REFERENCES

- [1] Lindmark M, Bergquist AK, Andersson LF. Energy transition, carbon dioxide reduction and output growth in the Swedish pulp and paper industry: 1973–2006. *Energy Pol* 2011;39(9):5449–56.
- [2] Zhang T, Liu J, Sun S. Technology transition from traditional oil and gas reservoir simulation to the next generation energy development. *Adv Geo-Energy Res* 2023;7(1):69–70.
- [3] Chen L, Msigwa G, Yang M, Osman AI, Fawzy S, Rooney DW, Yap PS. Strategies to achieve a carbon neutral society: a review. *Environ Chem Lett* 2022;20(4):2277–310.
- [4] Ishaq H, Dincer I, Crawford C. A review on hydrogen production and utilization: challenges and opportunities. *Int J Hydrogen Energy* 2022;47(62):26238–64.
- [5] Arsalis A, Papanastasiou P, Georgiou GE. A comparative review of lithium-ion battery and regenerative hydrogen fuel cell technologies for integration with photovoltaic applications. *Renew Energy* 2022;191:943–60.
- [6] Heinemann N, Alcalde J, Miocic JM, Hangx SJ, Kallmeyer J, Ostertag-Henning C. Enabling large-scale hydrogen storage in porous media—the scientific challenges. *Energy Environ Sci* 2021;14(2):853–64.
- [7] Arcos JMM, Santos DM. The hydrogen color spectrum: techno-economic analysis of the available technologies for hydrogen production. *Gas* 2023;3(1):25–46.
- [8] Abad AV, Dodds PE. Green hydrogen characterisation initiatives: definitions, standards, guarantees of origin, and challenges. *Energy Pol* 2020;138:111300.
- [9] Salehmin MNI, Husaini T, Goh J, Sulong AB. High-pressure PEM water electrolyser: a review on challenges and mitigation strategies towards green and low-cost hydrogen production. *Energy Convers Manag* 2022;268:115985.
- [10] Dao C, Kazemtabrizi B, Crabtree C. Wind turbine reliability data review and impacts on levelised cost of energy. *Wind Energy* 2019;22(12):1848–71.
- [11] Chae MJ, Kim JH, Moon B, Park S, Lee YS. The present condition and outlook for hydrogen-natural gas blending technology. *Kor J Chem Eng* 2022;39(2):251–62.
- [12] Howarth RW, Jacobson MZ. How green is blue hydrogen? *Energy Sci Eng* 2021;9(10):1676–87.
- [13] Diab J, Fulcheri L, Hessel V, Rohani V, Frenklach M. Why turquoise hydrogen will be a game changer for the energy transition. *Int J Hydrogen Energy* 2022;47(61):25831–48.
- [14] Huang J, Balcombe P, Feng Z. Technical and economic analysis of different colours of producing hydrogen in China. *Fuel* 2023;337:127227.
- [15] Kaitsu M, Swann T, Quicke A. Hydrogen-is hydrogen the next "clean coal". The Australia Institute; 2019.
- [16] Boretti A. Supply of abundant and low-cost total primary energy to a growing world needs nuclear energy and hydrogen energy storage. *Int J Hydrogen Energy* 2022;48(5):1649–50.
- [17] Taylor K. Hydrogen produced from nuclear will be considered 'low-carbon'. EU official says; 2020. Available from: <https://www.euractiv.com/section/energy->



- environment/news/hydrogen-produced-from-nuclear-will-be-considered-low-carbon-eu-official-says/.
- [18] Korányi TI, Németh M, Beck A, Horváth A. Recent advances in methane pyrolysis: turquoise hydrogen with solid carbon production. *Energies* 2022;15(17):6342.
  - [19] Ajanovic A, Sayer M, Haas R. The economics and the environmental benignity of different colors of hydrogen. *Int J Hydrogen Energy* 2022;47(57):24136–54.
  - [20] Rigollet C, Prinzhofer A. Natural hydrogen: a new source of carbon-free and renewable energy that can compete with hydrocarbons. *First Break* 2022;40(10):78–84.
  - [21] Tian QN, Yao SQ, Shao MJ, Zhang W, Wang HH. Origin, discovery, exploration and development status and prospect of global natural hydrogen under the background of “carbon neutrality”. *China Geology* 2022;5(4):722–33.
  - [22] Rasul MG, Hazrat MA, Sattar MA, Jahirul MI, Shearer MJ. The future of hydrogen: challenges on production, storage and applications. *Energy Convers Manag* 2022;272:116326.
  - [23] Zhang T, Sun S. Thermodynamics-informed neural network (TINN) for phase equilibrium calculations considering capillary pressure. *Energies* 2021;14(22):7724.
  - [24] Von Solms N, Jensen L, Kofod JL, Michelsen ML, Kontogeorgis GM. Measurement and modelling of hydrogen bonding in 1-alkanol+ n-alkane binary mixtures. *Fluid Phase Equil* 2007;261(1–2):272–80.
  - [25] Bell IH, Deiters UK, Jäger A. Algorithm to identify vapor–liquid–liquid equilibria of binary mixtures from vapor–liquid equilibria. *Ind Eng Chem Res* 2022;61(6):2592–9.
  - [26] Züttel A. Materials for hydrogen storage. *Mater Today* 2003;6(9):24–33.
  - [27] Krasae-in S, Stang JH, Neksa P. Development of large-scale hydrogen liquefaction processes from 1898 to 2009. *Int J Hydrogen Energy* 2010;35(10):4524–33.
  - [28] Skiba SS, Larionov EG, Manakov AY, Kolesov BA, Ancharov AI, Aladko EY. Double clathrate hydrate of propane and hydrogen. *J Inclusion Phenom Macrocycl Chem* 2009;63:383–6.
  - [29] Veluswamy HP, Yew JC, Linga P. New hydrate phase equilibrium data for two binary gas mixtures of hydrogen and propane coupled with a kinetic study. *J Chem Eng Data* 2015;60(2):228–37.
  - [30] Lopez-Lazaro C, Bachaud P, Moretti I, Ferrando N. Predicting the phase behavior of hydrogen in NaCl brines by molecular simulation for geological applications. *Bull Soc Geol Fr* 2019;190(1).
  - [31] Ferrando N, Ungerer P. Hydrogen/hydrocarbon phase equilibrium modelling with a cubic equation of state and a Monte Carlo method. *Fluid Phase Equil* 2007;254(1–2):211–23.
  - [32] Ma QL, Chen GJ, Sun CY. Vapor–liquid–liquid–hydrate phase equilibrium calculation for multicomponent systems containing hydrogen. *Fluid Phase Equil* 2013;338:87–94.
  - [33] Nichita DV. New unconstrained minimization methods for robust flash calculations at temperature, volume and moles specifications. *Fluid Phase Equil* 2018;466:31–47.
  - [34] Jindrová T, Mikyška J. Fast and robust algorithm for calculation of two-phase equilibria at given volume, temperature, and moles. *Fluid Phase Equil* 2013;353:101–14.
  - [35] Zhang T, Li Y, Li Y, Sun S, Gao X. A self-adaptive deep learning algorithm for accelerating multicomponent flash calculation. *Comput Methods Appl Mech Eng* 2020;369:113207.
  - [36] Liu T, Dong Z, Zhu W, Chen Y, Zhou M, Cui P. Prediction of the solubility of acid gas hydrogen sulfide in green solvent ionic liquids via quantitative structure–property relationship models based on the molecular structure. *ACS Sustainable Chem Eng* 2023;11(9):3917–31.
  - [37] Sharma P, Jain A, Bora BJ, Balakrishnan D, Show PL, Ramaraj R. Application of modern approaches to the synthesis of biohydrogen from organic waste. *Int J Hydrogen Energy* 2023;48(55):21189–213.
  - [38] Liu, T., Fan, D., Chen, Y., Dai, Y., Jiao, Y., Cui, P., ... & Zhu, Z. Prediction of CO<sub>2</sub> solubility in ionic liquids via convolutional autoencoder based on molecular structure encoding. *AIChE J*, e18182.
  - [39] Chen Z, Zhang Y, Zhou M, Yin K, Zhou Y, Cui P. Mechanism analysis and process optimization of acetone–methanol azeotrope separation using 1-ethyl-3-methylimidazolium acetate based mixed extractants. *J Clean Prod* 2022;379:134687.
  - [40] Qi H, Xu H, Zhang J, Xu Z, Zhong L, Cui P. Thermodynamic and techno-economic analyses of hydrogen production from different algae biomass by plasma gasification. *Int J Hydrogen Energy* 2023. In press.
  - [41] Yu E, Pan Y. First-principles prediction of structural, electronic and optical properties of alkali metals AM<sub>4</sub>BN<sub>3</sub>H<sub>10</sub> hydrides. *Int J Hydrogen Energy* 2023;48(39):14785–94.
  - [42] Pan Y, Guan W. Effect of sulfur concentration on structural, elastic and electronic properties of molybdenum sulfides from first-principles. *Int J Hydrogen Energy* 2016;41(26):11033–41.
  - [43] Pan Y, Yu E. New insight into the structural and physical properties of AlH<sub>3</sub>. *Int J Energy Res* 2022;46(14):19678–85.
  - [44] Sultana N, Hossain SZ, Aljameel SS, Omran ME, Razzak SA, Haq B, Hossain MM. Biohydrogen from food waste: modeling and estimation by machine learning based super learner approach. *Int J Hydrogen Energy* 2023;48(49):18586–600.
  - [45] Fan D, Xue K, Liu Y, Zhu W, Chen Y, Cui P. Modeling the toxicity of ionic liquids based on deep learning method. *Comput Chem Eng* 2023;176:108293.
  - [46] Lee J, Hong S, Cho H, Lyu B, Kim M, Kim J, Moon I. Machine learning-based energy optimization for on-site SMR hydrogen production. *Energy Convers Manag* 2021;244:114438.
  - [47] Hosseinzadeh A, Zhou JL, Altaee A, Li D. Machine learning modeling and analysis of biohydrogen production from wastewater by dark fermentation process. *Bioresour Technol* 2022;343:126111.
  - [48] Pan Y. First-principles investigation of structural stability, electronic and optical properties of suboxide (Zr<sub>3</sub>O). *Mater Sci* 2022;281:115746.
  - [49] Pan Y, Guan WM. Prediction of new phase and electrochemical properties of Li<sub>2</sub>S<sub>2</sub> for the application of Li-S batteries. *Inorg Chem* 2018;57(11):6617–23.
  - [50] Pan Y. Influence of oxygen vacancies on the electronic and optical properties of zirconium dioxide from first-principles calculations. *J Electron Mater* 2019;48(8):5154–60.
  - [51] Pan Y. Effects of Cu, Ag and Au on electronic and optical properties of  $\alpha$ -Ga<sub>2</sub>O<sub>3</sub> oxide according to first-principles calculations. *J Phys Chem Solid* 2023;174:111152.
  - [52] Chen S, Pan Y, Wang D, Deng H. Structural stability and electronic and optical properties of bulk WS<sub>2</sub> from first-principles investigations. *J Electron Mater* 2020;49:7363–9.
  - [53] Marcato A, Marchisio D, Boccardo G. Reconciling deep learning and first-principle modelling for the investigation of transport phenomena in chemical engineering. *Can J Chem Eng* 2023;101(6):3013–8.
  - [54] Li Y, Zhang T, Sun S. Acceleration of the NVT flash calculation for multicomponent mixtures using deep neural network models. *Ind Eng Chem Res* 2019;58(27):12312–22.
  - [55] Tian QN, Yao SQ, Shao MJ, Zhang W, Wang HH. Origin, discovery, exploration and development status and prospect

- of global natural hydrogen under the background of “carbon neutrality”. *China Geology* 2022;5(4):722–33.
- [56] Zgonnik V. The occurrence and geoscience of natural hydrogen: a comprehensive review. *Earth Sci Rev* 2020;203:103140.
- [57] Ward LK. Report on the prospects of obtaining supplies of petroleum by boring in the vicinity of Robe and elsewhere in the south-eastern portion of South Australia. *Geol Surv S Aust Report* 1917. Book No. 5/191.
- [58] Binary interaction paramters. <https://wiki.whitson.com/eos/bips/>.
- [59] Nichita DV, De-Hemptinne JC, Gomez S. Isochoric phase stability testing for hydrocarbon mixtures. *Petrol Sci Technol* 2009;27(18):2177–91.
- [60] Nichita DV. Fast and robust phase stability testing at isothermal-isochoric conditions. *Fluid Phase Equil* 2017;447:107–24.
- [61] Nichita DV, Valencia CDLAD, Gomez S. Volume-based thermodynamics global phase stability analysis. *Chem Eng Commun* 2006;193(10):1194–216.
- [62] Zhang T, Zhang Y, Katterbauer K, Al Shehri A, Sun S, Hoteit I. Phase equilibrium in the hydrogen energy chain. *Fuel* 2022;328:125324.
- [63] Boreham CJ, Edwards DS, Czado K, Rollet N, Wang L, van der Wielen S. Hydrogen in Australian natural gas: occurrences, sources and resources. *The APPEA Journal* 2021;61(1):163–91.
- [64] Kou J, Sun S. A stable algorithm for calculating phase equilibria with capillarity at specified moles, volume and temperature using a dynamic model. *Fluid Phase Equil* 2018;456:7–24.
- [65] Tan SP, Piri M. Equation-of-state modeling of confined-fluid phase equilibria in nanopores. *Fluid Phase Equil* 2015;393:48–63.
- [66] Chen Z, Huan G, Ma Y. Computational methods for multiphase flows in porous media. Society for Industrial and Applied Mathematics; 2006.
- [67] Sing KS, Williams RT. Historical aspects of capillarity and capillary condensation. *Microporous Mesoporous Mater* 2012;154:16–8.
- [68] Weinaug CF, Katz DL. Surface tensions of methane-propane mixtures. *Ind Eng Chem* 1943;35(2):239–46.
- [69] Ayirala SC, Rao DN. A new mechanistic Parachor model to predict dynamic interfacial tension and miscibility in multicomponent hydrocarbon systems. *J Colloid Interface Sci* 2006;299(1):321–31.
- [70] Wang L, Jin Z, Chen X, Su Y, Huang X. The origin and occurrence of natural hydrogen. *Energies* 2023;16(5):2400.
- [71] Zhang T, Sun S, Bai H. Thermodynamically-consistent flash calculation in energy industry: from iterative schemes to a unified thermodynamics-informed neural network. *Int J Energy Res* 2022;46(11):15332–46.
- [72] Gal Y, Ghahramani Z. Dropout as a bayesian approximation: representing model uncertainty in deep learning. In: International conference on machine learning. PMLR; 2016, June. p. 1050–9.
- [73] Santurkar S, Tsipras D, Ilyas A, Madry A. How does batch normalization help optimization? *Adv Neural Inf Process Syst* 2018:31.
- [74] Kumar SK. On weight initialization in deep neural networks. arXiv preprint arXiv:1704.08863 2017.
- [75] Jin Xiaowei, et al. NSFnets (Navier-Stokes flow nets): physics-informed neural networks for the incompressible Navier-Stokes equations. *J Comput Phys* 2021;426:109951.